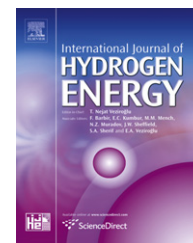


Available online at www.sciencedirect.com

SciVerse ScienceDirect

journal homepage: www.elsevier.com/locate/hydro

Numerical simulation of hydrogen impinging jet flame using flamelet generated manifold reduction

K.K.J. Ranga Dinesh^{a,*}, X. Jiang^a, J.A. van Oijen^b^a Engineering Department, Lancaster University, Lancaster, Lancashire LA1 4YR, UK^b Combustion Technology, Department of Mechanical Engineering, Eindhoven University of Technology, Eindhoven, The Netherlands

ARTICLE INFO

Article history:

Received 24 September 2011

Received in revised form

26 November 2011

Accepted 30 November 2011

Available online 23 December 2011

Keywords:

Hydrogen combustion

Impinging jet

Buoyancy

DNS

FGM

ABSTRACT

A transitional hydrogen–air non-premixed impinging jet flame is studied using three-dimensional direct numerical simulation (DNS) and flamelet generated manifolds (FGM) based on detailed chemical kinetics. The simulations are used to investigate the buoyancy instability and the spatial and temporal patterns of the impinging jet flame. The computational domain employed has a size of 4 jet diameters in the streamwise direction and 12 jet diameters in the cross-streamwise direction. The results presented in this study were performed using a uniform Cartesian grid with $200 \times 600 \times 600$ points. Reynolds number used was $Re = 2000$, based on the inlet reference quantities. The spatial discretisation was carried out using a sixth-order accurate compact finite difference scheme and the discretised equations were advanced in time using a third-order accurate fully explicit compact-storage Runge–Kutta scheme. Results show that the buoyancy and jet shear instability lead to form both inner and outer vortical structures in the primary and wall jet regions, thus complex spatial and temporal variations occur in the mixture fraction, progress variable and temperature fields. Moreover, DNS results suggest that the near-wall vortical structures play an important role in the near-wall heat transfer. These findings may provide useful guidelines for the near-wall combustion modelling using Reynolds-averaged Navier–Stokes modelling or large eddy simulation techniques.

Crown Copyright © 2011, Hydrogen Energy Publications, LLC. Published by Elsevier Ltd. All rights reserved.

1. Introduction

The environmental issues concerning the reduction of greenhouse gases from power-generating system has prompted researchers towards consideration of alternative fuel sources for energy conversion. The ongoing development of hydrogen technology as the appropriate type of energy for the future is an essential part of the clean energy strategy. Considerable effort is being directed towards updating safety codes and standards in preparation for production, distribution, and retail of hydrogen as a consumer energy source [1]. In

this context, combustion of hydrogen plays a tremendous role which seeks to provide a drive technology to fulfil current and future demand for individual mobility without the direct burning of fossil fuels. It is a well-known fact today that mankind needs alternatives to the consumption of fossil fuels, which are diminishing because of the continuous consumption and their limited availability. Contrary to such conventional fuels, hydrogen has a potential to meet the requirement of the future in full in both its generation and its sustainability, being embedded in the regenerating cycle of the nature. Hydrogen may be recovered from biomass and other

* Corresponding author. Tel.: +44 (0) 1524 594578.

E-mail address: ranga.dinesh@lancaster.ac.uk (K.K.J. Ranga Dinesh).

renewable resources, or even from nuclear processes. It can also be generated from fossil fuels such as natural gas, biogas, or other sources of primary energy. Depending on the development of its production technology, hydrogen may be available in virtually infinite supply. The exclusion of harmful emissions such as carbon dioxide and carbon monoxide, soot and unburned hydrocarbons makes burning of hydrogen perfect for clean combustion.

Various investigations have been carried out on developing an infrastructure for the future hydrogen economy involving safety standards [2], flame stability [3], fuel variability [4], etc. In addition various experimental and numerical investigations on specific areas of hydrogen combustion have also been carried out. Some of these studies include experimental investigations on the presence of barrier walls for hydrogen combustion [5,6], numerical calculations of accidental hydrogen release [7] and large-scale hydrogen detonation [8], characterisation of high-pressure hydrogen jet flames [9], numerical modelling of hydrogen triple flame [10] and emission analysis of hydrogen combustion in gas turbine feedstocks [11].

Hydrogen as a fuel is unique because of its simple oxidation kinetics, very large mass diffusivity and low molecular weight. Importantly, all chemical reactions that consume molecular hydrogen produce atomic hydrogen, which is an extremely reactive and diffusive species. It is also well known that the chemistry of hydrogen combustion is simpler than the combustion chemistry of other fuels, which may provide an advantage for combustion control. From a mathematical point of view, hydrogen combustion needs no more than six global chemical steps [12]. There are still uncertainties in the values of rate parameters of elementary steps of hydrogen combustion, but those uncertainties are less for hydrogen than for other fuels. There are different hydrogen–oxygen kinetic mechanisms in the literature. Westbrook and Dryer [13] reviewed the chemical kinetic modelling of high temperature hydrogen oxidation with emphasis on the hierarchical structure of reaction mechanisms for complex fuels. Saxena and Williams [14] tested a detailed and reduced chemical kinetic mechanisms for hydrogen combustion and Williams [12] further extended the work for hydrogen auto-ignition.

Impinging non-premixed combustion is encountered in a broad range of practical industrial systems where the flames may induce various effects on the overall efficiency and pollutant formation of the combustion, as well as the lifetime of the combustion chambers [15]. Buoyancy effects due to the interaction between the density or temperature inhomogeneity and gravity are important in relatively low speed flames. Because of the importance of buoyancy and wall boundaries in combustion applications, identification of the dynamics driven by buoyancy such as mixing and entrainment characteristics and interaction between flame and wall makes impinging non-premixed jet flame fundamentally important for the understanding of combustion systems. Despite having a relatively simple geometry, buoyancy driven impinging reacting jets offer great value in the study of fundamental physical concepts such as large and small scale vortices, flame–wall interactions, wall boundary layers, wall heat transfer, and intermittency, etc. [16]. Because of the wealthy flow phenomena involved and the geometric simplicity,

impinging flames can be a benchmark for the development and validation of near-wall models [17,18]. In buoyant flows, the periodic vortex shedding often referred to as flickering has been well known, which may subject to various other instabilities including the shear instability that can be independent to the buoyancy instability. Buoyancy instability normally leads to the formation of outer vortical structures and shear instability leads to the formation of inner vortical structures, while the boundary walls can also modify the vortex topology significantly in impinging jet flames.

In recent years significant progress has been made in computational research of turbulent combustion, e.g. [19]. Direct numerical simulation (DNS) has emerged as the most promising technical tool to fundamentally simulate turbulent combustion problems, in which all relevant continuum scales are resolved which can discover complex scientific and technological issues, and help model developments for large eddy simulation (LES) and Reynolds-averaged Navier–Stokes (RANS) modelling techniques. Historically, most DNS flame analyses were based on simple chemistry, but the continuous growth in computing power has been tremendously helpful in incorporating detailed combustion chemistry and large-scale DNS in computational combustion. Early investigations reported two-dimensional simulations of non-premixed flames [20,21]. Since most combustion problems are three-dimensional in nature and two-dimensional/axisymmetric simulations only capture the cross-streamwise or the azimuthal vorticity and exclude the streamwise vorticity development, it is important to consider full three-dimensional simulations to capture essential flow characteristics. Three-dimensional effects, such as helical modes or flapping modes, can often be triggered by small perturbations existing in the combusting flame surroundings and lead to toroidal-like vortices in the flow field, vastly changing the vortex dynamics and flame behaviour. Furthermore in DNS, it is also important to include realistic flame chemistry in the simulations so that the solutions will give near-exact solutions of the reacting flow fields.

Recently DNS calculations have certainly added a great deal of understanding, providing fundamental answers to many benchmark combustion problems. Mahalingam et al. [22] performed three-dimensional DNS of turbulent non-premixed flame including finite rate chemistry and heat release effects. Since then various research groups have focused on DNS of non-premixed combustion and analysed turbulence chemistry interaction, fuel variability and flame stabilisation, local extinction, auto-ignition etc. For example, Im and Chen [23] studied the effect of flow strain on an hydrogen–air triple flame using DNS, while Dabireau et al. [24] performed one-dimensional (1D) simulation of hydrogen combustion interacting with an inert wall. Hawkes et al. [25] carried out scalar intermittency of CO/H₂ planar jet flame using DNS, while Yoo et al. [26] performed DNS for flame stabilisation and structure of lifted hydrogen jet flame. Recently Gruber et al. [27] studied turbulent flame–wall interaction for hydrogen–air premixed flame using DNS, while Pitsch [28] has further demonstrated the importance of investigating near-wall combustion using DNS.

Although much research including experimental and theoretical studies has been carried out on hydrogen

combustion, buoyancy effects on hydrogen flames in an impinging configuration have not been fully investigated. However, hydrogen or other hydrogen enriched fuels such as syngas combustion is highly buoyant, which as a research topic has gained an increasing amount of attention in recent years due to its usage in a range of combustion systems such as combustion engines, gas turbine combustors and other industrial processes. In this paper, we present a fundamental investigation aiming to identify the vortical structures, flame characteristics, and near-wall combustion of hydrogen impinging jet for a transitional impinging jet using direct numerical simulation and detailed chemical kinetics. The aim here is to demonstrate the important physics of shear layer instability, buoyancy instability and combination of shear and buoyancy instability of a hydrogen impinging jet using DNS technique and FGM approach, as a means to reduce the prohibitive computational costs of directly implementing detailed chemistry in a DNS code. This is the first step of a series of investigations aiming for understanding the flame characteristics of hydrogen enriched fuel mixtures, and understanding the near-wall turbulent vortical structures and wall heat transfer using advanced DNS and FGM approach. The detailed chemical kinetics has been employed through the FGM method [29], which not only uses complex chemistry, but also takes the most important transport processes into account. The buoyancy instability has been investigated by switching on or off its effects in the simulations performed. The results are discussed in terms of distributions of instantaneous velocity field, mixture fraction, progress variable and flame temperature and frequency spectra. Five sections will follow. The next section discusses the DNS governing equations followed by the chemistry and FGM approach in Section 3. Section 4 describes the numerical approach followed by the results and discussion in Section 5. Section 6 summarises the results and presents the conclusions.

2. DNS governing equations

The governing equations for the reacting flow field are based on fundamental laws of conservation. The conservation equations for mass, momentum, energy, mixture fraction and transport equation for the progress variable in their original dimensional form can be given as:

$$\frac{\partial \rho^*}{\partial t^*} + \frac{\partial (\rho^* u_j^*)}{\partial x_j^*} = 0, \quad (1)$$

$$\frac{\partial (\rho^* u_j^*)}{\partial t^*} + \frac{\partial (\rho^* u_j^* u_k^* + p^* \delta_{jk})}{\partial x_k^*} - \frac{\partial \tau_{jk}^*}{\partial x_k^*} + (\rho_a^* - \rho^*) g_j^* = 0, \quad (2)$$

$$\frac{\partial \rho^* e^*}{\partial t^*} + \frac{\partial [(\rho^* e^* + p^*) u_k^*]}{\partial x_k^*} + \frac{\partial q_k^*}{\partial x_k^*} - \frac{\partial (u_j^* \tau_{jk}^*)}{\partial x_k^*} + (\rho_a^* - \rho^*) g_k^* u_k^* = 0, \quad (3)$$

$$\frac{\partial (\rho^* Y^*)}{\partial t^*} + \frac{\partial (\rho^* u_k^* Y^*)}{\partial x_k^*} - \frac{\partial}{\partial x_k^*} \left(\rho^* D_Y^* \frac{\partial Y^*}{\partial x_k^*} \right) - \omega_Y^* = 0, \quad (4)$$

$$\frac{\partial (\rho^* Z^*)}{\partial t^*} + \frac{\partial (\rho^* u_k^* Z^*)}{\partial x_k^*} - \frac{\partial}{\partial x_k^*} \left(\rho^* D_Z^* \frac{\partial Z^*}{\partial x_k^*} \right) = 0, \quad (5)$$

$$p^* = \rho^* R^* T^*. \quad (6)$$

In Eqs. (1)–(6), t stands for time, u_j is the velocity components in the x_j direction, e stands for total energy per unit mass, p stands for pressure, λ stands for heat conductivity, C_p stands for specific heat at constant pressure, μ stands for dynamic viscosity, γ is the ratio of specific heats, ω_Y is the source term of the progress variable, ρ is the density, subscript a stands for the ambient, respectively. Here the superscript $*$ stands for dimensional quantities.

Viscous effects are represented by the stress tensor τ . Ignoring differential diffusion effects, the heat flux is given by

$$q_k^* = -\lambda^* \frac{\partial T^*}{\partial x_k^*} \quad (7)$$

In general, the transport coefficients are complicated functions of temperature and chemical composition of the mixture. In the FGM approach, the transport coefficients μ and λ are stored in the FGM data table. Assuming unity Lewis number, the diffusion coefficients for Y and Z are given by

$$\rho^* D_Y^* = \rho^* D_Z^* = \frac{\lambda^*}{C_p} \quad (8)$$

where C_p is the specific heat capacity at constant pressure.

Therefore the governing equations can be re-arranged as:

$$\frac{\partial \rho^*}{\partial t^*} + \frac{\partial (\rho^* u_j^*)}{\partial x_j^*} = 0, \quad (9)$$

$$\frac{\partial (\rho^* u_j^*)}{\partial t^*} + \frac{\partial (\rho^* u_j^* u_k^* + p^* \delta_{jk})}{\partial x_k^*} - \frac{\partial \tau_{jk}^*}{\partial x_k^*} + (\rho_a^* - \rho^*) g_j^* = 0, \quad (10)$$

$$\frac{\partial \rho^* e^*}{\partial t^*} + \frac{\partial [(\rho^* e^* + p^*) u_k^*]}{\partial x_k^*} - \frac{\partial}{\partial x_k^*} \left(\lambda^* \frac{\partial T^*}{\partial x_k^*} \right) - \frac{\partial (u_j^* \tau_{jk}^*)}{\partial x_k^*} + (\rho_a^* - \rho^*) g_k^* u_k^* = 0, \quad (11)$$

$$\frac{\partial (\rho^* Y^*)}{\partial t^*} + \frac{\partial (\rho^* u_k^* Y^*)}{\partial x_k^*} - \frac{\partial}{\partial x_k^*} \left(\frac{\lambda^*}{C_p} \frac{\partial Y^*}{\partial x_k^*} \right) - \omega_Y^* = 0, \quad (12)$$

$$\frac{\partial (\rho^* Z^*)}{\partial t^*} + \frac{\partial (\rho^* u_k^* Z^*)}{\partial x_k^*} - \frac{\partial}{\partial x_k^*} \left(\frac{\lambda^*}{C_p} \frac{\partial Z^*}{\partial x_k^*} \right) = 0, \quad (13)$$

$$p^* = \rho^* R^* T^*. \quad (14)$$

In this study, the governing equations are solved in terms of their non-dimensional form in order to facilitate the analysis of the reacting flow physics. A set of dimensionless variables are defined in terms of the dimensional counterparts by the relations given in Table 1, where the superscript $*$ stands for the reference quantities which has been omitted for brevity when subscript 0 is used.

Major reference quantities used in the normalisation are l_0 – diameter of the impinging jet, u_0 – the maximum velocity of the fuel jet at the source on the inlet plane, $g_0 = 9.81 \text{ ms}^{-2}$, T_0 – the ambient temperature, ρ_0 – fuel density at ambient

Table 1 – Definition of dimensionless variables.

Time	Spatial coordinates	Velocity
$t = \frac{t^*}{t_0}$	$x = \frac{x^*}{l_0}$	$u = \frac{u^*}{u_0}$
Density	Pressure	Temperature
$\rho = \frac{\rho^*}{\rho_0}$	$p = \frac{p^*}{\rho_0 u_0^2}$	$T = \frac{T^*}{T_0}$
Internal energy	Viscosity	Thermal conductivity
$e = \frac{e^*}{e_0}$	$\mu = \frac{\mu^*}{\mu_0}$	$\lambda = \frac{\lambda^*}{\lambda_0}$
Gravity	Specific heat capacity	Source term of the progress variable
$g = \frac{g^*}{g_0}$	$C_p = \frac{C_p^*}{C_{p_0}}$	$\omega_Y = \frac{\omega_Y^* \rho_0 Y_0}{t_0}$
Reynolds number	Prandtl number	Froude number
$Re = \frac{\rho_0 u_0 l_0}{\mu_0}$	$Pr = \frac{\mu_0 C_{p_0}}{\lambda_0}$	$Fr = \frac{u_0^2}{g_0^2 l_0}$
Mach number		
$M = \frac{u_0}{\sqrt{\gamma R_0 T_0}}$		

temperature, μ_0 – fuel viscosity at ambient temperature, λ_0 – fuel thermal conductivity at ambient temperature and C_{p_0} – fuel specific heat at constant pressure at ambient temperature.

According to the aforementioned reference quantities, the final normalised governing equations can be written as follows:

$$\frac{\partial \rho}{\partial t} + \frac{\partial(\rho u_j)}{\partial x_j} = 0, \quad (15)$$

$$\frac{\partial(\rho u_j)}{\partial t} + \frac{\partial(\rho u_j u_k)}{\partial x_k} + \frac{\partial p}{\partial x_k} - \frac{1}{Re} \frac{\partial \tau_{jk}}{\partial x_k} + (\rho_a - \rho) \frac{g_j}{Fr} = 0, \quad (16)$$

$$\begin{aligned} \frac{\partial \rho e}{\partial t} + \frac{\partial(\rho e u_k)}{\partial x_k} + \frac{\partial(p u_k)}{\partial x_k} - \frac{1}{Re} \frac{\partial}{\partial x_k} \left(\frac{\lambda}{C_p} \frac{\partial T}{\partial x_k} \right) \\ - \frac{1}{Re} \frac{\partial(u_j \tau_{jk})}{\partial x_k} + (\rho_a - \rho) \frac{g_k u_k}{Fr} = 0, \end{aligned} \quad (17)$$

$$\frac{\partial(\rho Y)}{\partial t} + \frac{\partial(\rho u_k Y)}{\partial x_k} - \frac{1}{Re} \frac{\partial}{\partial x_k} \left(\frac{\lambda}{C_p} \frac{\partial Y}{\partial x_k} \right) - \omega_Y = 0, \quad (18)$$

$$\frac{\partial(\rho Z)}{\partial t} + \frac{\partial(\rho u_k Z)}{\partial x_k} - \frac{1}{Re} \frac{\partial}{\partial x_k} \left(\frac{\lambda}{C_p} \frac{\partial Z}{\partial x_k} \right) = 0, \quad (19)$$

$$p = \frac{\rho T}{\gamma M^2} \quad (20)$$

Here M , Pr , Fr and Re represent Mach number, Prandtl number, Froude number and Reynolds number, respectively.

3. Chemistry and flamelet generated manifolds (FGMs)

The flame chemistry must be realistically represented in order to accurately predict the chemical heat release and the concentrations of the chemical species of the hydrogen combustion. However, it is computationally expensive to incorporate a detailed chemical mechanism into direct numerical simulation due to the large computer memory and

CPU requirements. Therefore several reduction chemistry mechanisms have been developed and applied for large-scale numerical calculations. For example, the systematic reduction technique [30], the intrinsic low dimensional manifolds technique [31], and the computational singular perturbation method [32] have been applied as reduction chemistry mechanisms for numerical simulations. However, these reduction techniques mainly developed using chemistry only and do not take the transport process into account. This can be identified as a drawback particularly in low temperature regions of the flame where both chemistry and transport are important [33]. In this work, the flame chemistry of H_2 –Air combustion is represented by the database of FGM technique developed by van Oijen and Goey [29], which account both chemical and transport processes as a function of mixture fraction and progress variable while sharing the laminar flamelet concept developed by Peters [34]. However, if we neglect transport properties such as viscosity, thermal conductivity as a function of mixture fraction and progress variable in the FGM table, these transport variables should be calculated using appropriate formulations. This leads to increase the computational costs as additional equations have to be solved. Therefore the inclusion of both chemical and transport properties into FGM table not only provide meaningful physical representation, but also reduce the computational cost for a large-scale DNS calculation. In this way, the H_2 –Air chemically reacting flow is computed without incurring significant computational expenses due to the flame chemistry.

In the present study, the FGM database has been generated for the H_2 –Air system based on counter-flow non-premixed flamelets. The flamelets have been computed by using detailed chemistry [35] and transport models including differential diffusion effects. The mass fraction of H_2O is selected as the progress variable. The database contains the variables as a function of the mixture fraction Z and the progress variable Y such that (the superscript * for all these dimensional quantities has been dropped for brevity):

$$\omega_Y = \omega_Y^{FGM}(Y, Z) \quad \text{kg/m}^3\text{s} \quad (21)$$

$$R_g = R_g^{FGM}(Y, Z) \quad \text{J/kg K} \quad (22)$$

$$C_p = C_p^{FGM}(Y, Z) \quad \text{J/kg K} \quad (23)$$

$$h - C_p T = (h - C_p)^{FGM}(Y, Z) \quad \text{J/kg} \quad (24)$$

$$\mu = \mu^{FGM}(Y, Z) \quad \text{kg/ms} \quad (25)$$

$$\lambda = \lambda^{FGM}(Y, Z) \quad \text{W/mK} \quad (26)$$

In Eqs. (21)–(26), R_g and h stand for gas constant and enthalpy, respectively. The flame temperature is obtained by linearising the enthalpy around the state on the manifold, which leads to an explicit expression. The calorific equation of state reads

$$e = h - \frac{p}{\rho} + \frac{1}{2} u_k u_k \quad (27)$$

with

$$h = h^{\text{ref}} + \int_{T^{\text{ref}}}^T C_p d\eta \quad (28)$$

Here η represents temperature. Since heat capacity C_p is in general not a constant, but a function of temperature and mixture composition, the temperature T has to be determined in an iterative way. To simplify this, the enthalpy h is linearised around the state on the manifold such that

$$h(T) \approx h^{\text{FGM}} + C_p^{\text{FGM}}(T - T^{\text{FGM}}) \quad (29)$$

Substitution into (27) gives

$$e = h^{\text{FGM}} + C_p^{\text{FGM}}(T - T^{\text{FGM}}) - R_g^{\text{FGM}}T + \frac{1}{2}u_k u_k \quad (30)$$

It leads to an explicit expression for temperature:

$$T = \frac{(e - 1/2 u_k u_k) - (h - C_p T)^{\text{FGM}}}{C_p^{\text{FGM}} - R_g^{\text{FGM}}} \quad (31)$$

The heat capacity C_p and the term $(h - C_p T)$ are stored in the FGM table.

Fig. 1 shows the non-premixed manifolds, which results from the one-dimensional flamelet calculations and which serve as input for the three-dimensional (3D) DNS for

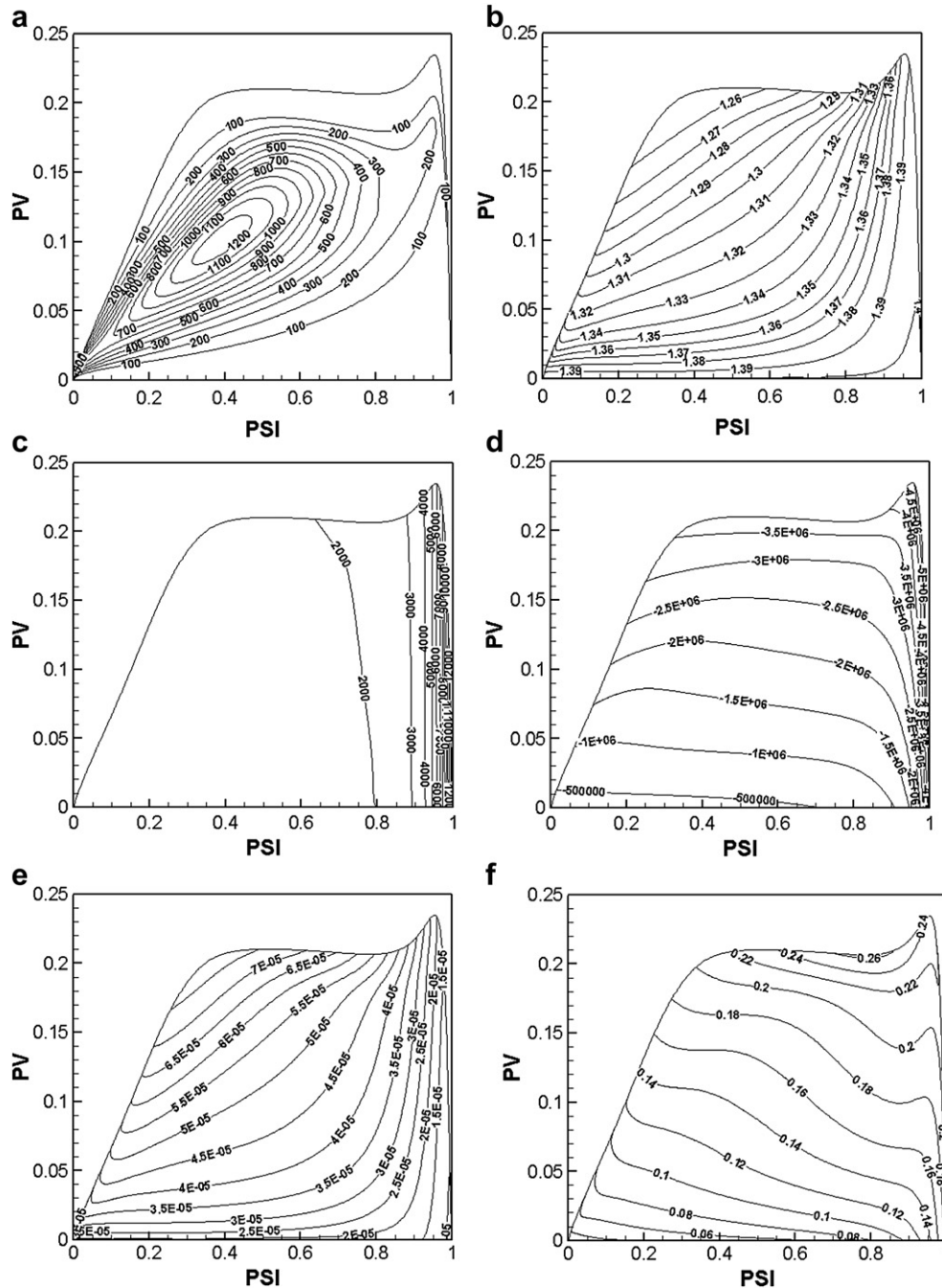


Fig. 1 – Hydrogen–air non-premixed manifolds for (a) source term of the progress variable S_p , (b) ratio of specific heats γ , (c) specific heat at constant pressure C_p , (d) variable $H - C_p T$, (e) viscosity μ , and (f) thermal conductivity λ .

variables: source term of the progress variable S_p , ratio of specific heats γ , specific heat at constant pressure C_p , variable $H - C_p T$, viscosity μ and thermal conductivity λ as a function of equidistant mixture fraction (PSI) and progress variable (PV). The resolution of the manifolds is 301 points in the mixture fraction direction and 101 points in the progress variable direction. The points in mixture fraction direction are distributed equidistantly in PSI space where $PSI = Z/[Z + a(1 - Z)]$ with $a = Z_{st}/(1 - Z_{st})$. This results in a high resolution in the region with the highest activity near $Z = Z_{st} = 0.028$. Bilinear interpolation is employed when this manifold is accessed in the DNS calculation to return values of above noted dependent variables for the local values of mixture fraction and progress variable.

4. Numerical approach

4.1. Discretisation

In the present work, a non-premixed hydrogen impinging jet has been simulated using DNS with the flame chemistry represented by the tabulated FGM approach. Three-dimensional time-dependent Navier–Stokes equations in the Cartesian coordinate system have been solved in their non-dimensional form. The computational domain employed has a size of four jet nozzle diameters in the streamwise direction and twelve jet nozzle diameters in the cross-streamwise direction. The results presented in this study were performed using a uniform Cartesian grid with $200 \times 600 \times 600$ points resulting 72 million nodes. The Reynolds number used was $Re = 2000$ based on the inlet reference quantities. The Prandtl number Pr and the specific heat γ vary according to the FGM table.

The discretisation of the governing equations includes the high-order numerical schemes for both spatial discretisation and time advancement. The spatial derivatives in all three directions are solved using a sixth-order accurate compact finite difference (Padé) scheme [36]. The finite difference scheme allows flexibility in the specification of boundary conditions for minimal loss of accuracy relative to spectral methods. The scheme uses sixth-order at inner points, fourth-order next to the boundary points, and third-order at the boundary. The Padé 3/4/6 scheme is arranged in a way that the sixth-order accuracy is achieved at the inner points by a compact finite differencing. For a general variable ϕ_i at grid point i in the x -direction, the first and second derivatives can be written in the following form:

$$\phi'_{i-1} + 3\phi'_i + \phi'_{i+1} = \frac{7}{3} \frac{\phi_{i+1} - \phi_{i-1}}{\Delta\eta} + \frac{1}{12} \frac{\phi_{i+2} - \phi_{i-2}}{\Delta\eta}, \quad (32)$$

$$\phi''_{i-1} + \frac{11}{2} \phi''_i + \phi''_{i+1} = 6 \frac{\phi_{i+1} - 2\phi_i + \phi_{i-1}}{\Delta\eta^2} + \frac{3}{8} \frac{\phi_{i+2} - 2\phi_i + \phi_{i-2}}{\Delta\eta^2}. \quad (33)$$

In Eqs. (32) and (33), $\Delta\eta$ is the cell size in the x -direction and cell sizes are uniform in all three directions. Further details of the Padé 3/4/6 scheme can be found in reference [36]. Solutions for the spatial discretised equations are obtained by solving the tridiagonal system of equations. The spatial

discretised equations are advanced in time using a fully explicit low-storage third-order Runge–Kutta scheme [37]. The time step was limited by the Courant number for stability and a chemical restraint.

4.2. Grid resolution and boundary conditions

The computational domain contains an inlet and impinging wall boundaries in the streamwise direction where the buoyancy force is acting. Fig. 2 shows the geometry of the impinging configuration considered here and the dimensions of the computational box used were $L_y = L_z = 12.0$ and $L_x = 4.0$. Since we focus on flame dynamics and near-wall flame development in the presence of buoyancy, we have employed the domain of $L_x = 4.0$ in the streamwise direction and $L_y = L_z = 12.0$ in the cross-streamwise direction. The present computational domain has been selected to ensure that the effects of buoyancy and the wall can be examined with affordable computational costs. At the inlet, the mean streamwise velocity was specified using a hyperbolic tangent profile $\bar{u} = U_{fuel}/2\{1 - \tanh[(0.5/4\delta)(r/0.5 - 0.5/r)]\}$ with $r = \sqrt{(z - 0.5L_z)^2 + (y - 0.5L_y)^2}$ where r stands for the radial direction of the round jet, originating from the centre of the inlet domain ($0 \leq x \leq L_x, 0 \leq y \leq L_y$) and the initial momentum thickness δ was chosen to be 10% of the jet radius. At the inflow, the flow was specified using the Navier–Stokes characteristic boundary conditions (NSCBC) [38] with the temperature treated as a soft variable (temperature was allowed to fluctuate according to the characteristic waves at the boundary). External unsteady disturbances were artificially added for all three velocity component at the inlet in sinusoidal form such that $u' = v' = w' = A \sin(2\pi f_0 t)$, which were added to the mean velocity profile. Here we assigned

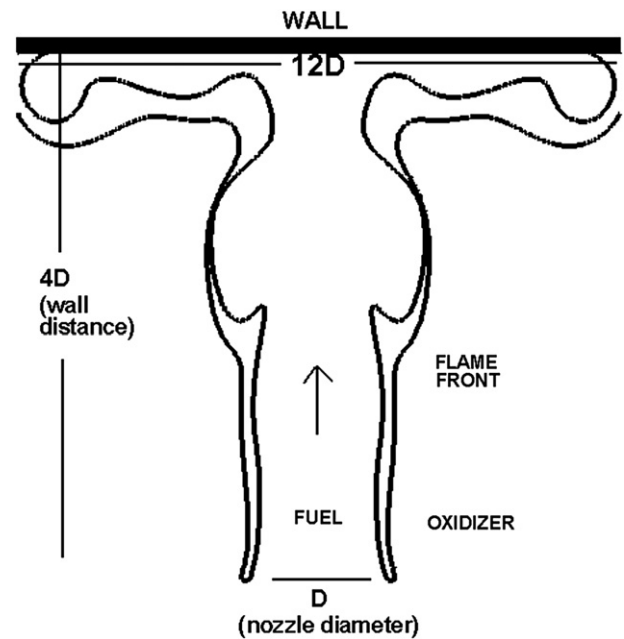


Fig. 2 – Geometry of the impinging flame with dimensions of 4 jet diameters in the streamwise direction and 12 jet diameters in the cross-streamwise direction.

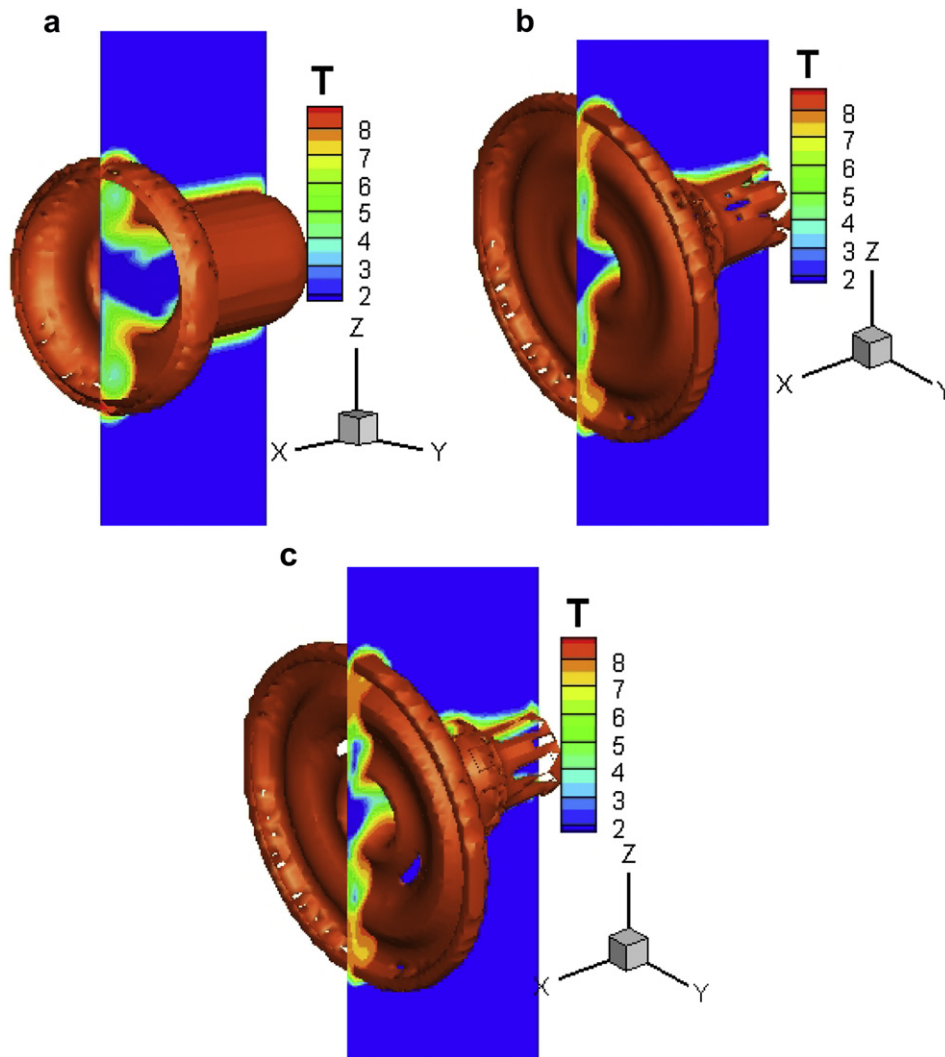


Fig. 3 – Instantaneous 3D iso-surfaces (iso-value = 8.4) and 2D contour plots of the flame temperature of cases A, B and C at $t = 16$. Here T represents the non-dimensional temperature (the non-dimensional temperature at the stoichiometric region (stoichiometric mixture fraction = 0.0285) reaches $T = 8.4$, which is around 2460 K).

the value $A = 0.05$ and the non-dimensional frequency of the unsteady disturbance $f_0 = 0.3$. In this study, the relatively large disturbance was used to enhance the development of instability in the computational domain, which is rather small in the streamwise direction, while the frequency of the perturbation was chosen to trigger the unstable mode of the jet. The non-slip wall boundary condition is applied at the solid wall, which is assumed to be at the ambient temperature and impermeable to mass. At the impinging wall boundary, the mixture fraction is assumed zero-gradient corresponding to the impermeability, while the progress variable for chemistry is taken as zero at the wall boundary. However, to further analyse the wall boundary conditions especially for the reaction progress variable, we intend to use FGM employing a modified source term of the progress variable as a function of mixture fraction, progress variable and enthalpy to account for possible wall heat losses in future studies. This will address the effect of heat loss on the source term as this effect can be important for the

calculation of the heat fluxes through the wall at more realistic conditions.

5. Results and discussion

This section presents descriptions of the effects of buoyancy and external perturbation on the hydrogen impinging jet flame. Comparisons are made between three cases: a non-buoyant case and two buoyant cases. Case A: a non-buoyant case with Froude number = infinity, with 5% perturbation applied to the three velocity components at the inlet; Case B: a buoyant case with Froude number = 1.0, with the inlet undisturbed; and Case C: another buoyant case with Froude number = 1.0, with the same inlet perturbation as Case A. The intention was to study the shear instability, buoyancy instability and combination of shear and buoyancy instability where both buoyancy and inertial momentum are important by analysing instantaneous velocity field, mixture fraction,

progress variable and flame temperature. Subsequently, Fourier spectra of the instantaneous streamwise velocity variation and Nusselt number distributions are also presented aiming for further analysis of the dynamics and near-wall combustion for the hydrogen non-premixed impinging flame.

Fig. 3 shows the instantaneous 3D iso-surfaces and two-dimensional (2D) contour plots of the flame temperature at $t = 16$ of cases A, B and C, respectively. The considered iso-surface value for all three cases is the non-dimensional flame temperature in the FGM database, $T = 8.4$ which is equal to $T = 2460$ K. The 3D plots of flame temperature show that the impinging jet defects from the wall and then convects along the surface of the wall, while the 2D results indicate that there is a non-reacting zone inside the jet where the temperature remains at the ambient value because of the unmixedness of the fuel with its ambient. The jet impingement forms a stagnation point, where the flow has zero velocity. The results exhibit typical flow features of impinging jets with the presence of both the primary jet stream and the wall jet.

Fig. 4 shows a series of snapshots of 2D cross-sectional instantaneous velocity vector fields of cases A, B and C at $t = 8, 12$ and 16 . As seen in Fig. 4(a1), (a2) and (a3), the symmetry of the non-buoyant case is breaking with respect to time and the asymmetric behaviour is propagating downwards. The flow field is predominately laminar-like. It is observed that the 5% external perturbation plays a significant role in the flow structure, which will in turn affect the

transport of scalars such as mixture fraction and progress variable as those shown subsequently. Furthermore, the development of two rotating vortices, i.e. the head vortices, can be seen at the wall jet for the non-buoyant case. Fig. 4(b1), (b2) and (b3) display the instantaneous velocity vector fields for case B. Compared with the non-buoyant case, the buoyant without inlet disturbance case exhibits significantly different flow structure. The instantaneous velocity fields show large differences in the shear layers of the primary jet and vortex formation at the wall jet. Complex large vortical structures associated with the buoyancy instability, which is known to trigger the flickering or puffing phenomenon, dominate the entrainment process, which will affect the distributions of mixture fraction, progress variable and flame temperature. It can be observed that the velocity puff in the near field moves upwards with respect to time. Similar behaviour is also observed in the wall jet region. For this buoyant case, it seems that vortical structures are formed in both the inner and outer sides of the primary jet stream and they dominate the entrainment process and thus affect the flow structure. The buoyancy instability leads to form large vortical structures, which are convected by the momentum of the primary jet stream as well as by the momentum of the secondary wall jet. The main reason for vorticity generation in the near-wall region is the external skin friction that acts on the thin layer of the fluid attached to the wall. The wall jet vortices move radially along the wall and reach the far-side location at $t = 12$. Fig. 4(c1), (c2) and (c3) show the time development of velocity

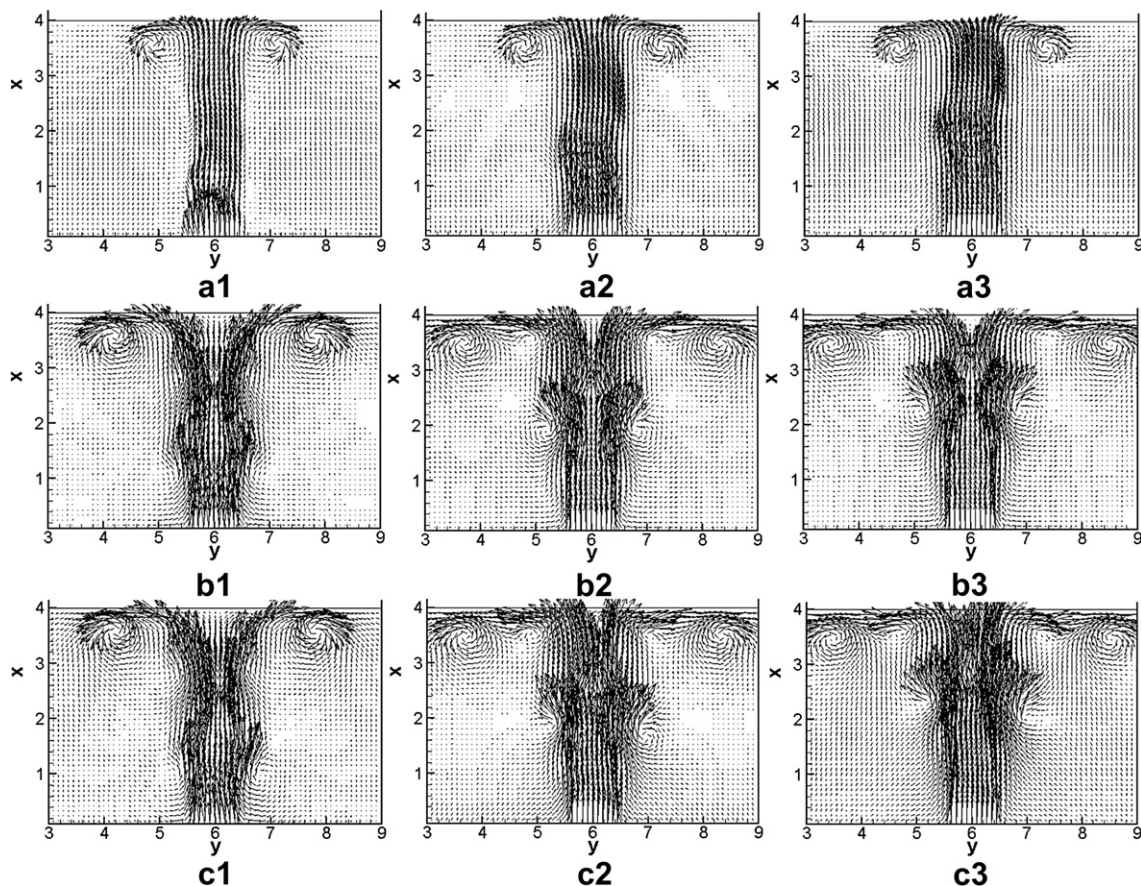


Fig. 4 – Instantaneous velocity vector fields of cases A, B and C at $t = 8$ (a1, b1, c1), $t = 12$ (a2, b2, c2) and $t = 16$ (a3, b3, c3).

vector fields for the buoyant with 5% inlet disturbance case. Compared with the undisturbed buoyant case, the disturbed buoyant case exhibits asymmetric behaviour of the primary jet and stronger vortical structures, because of the external perturbation applied at the jet nozzle exit.

Snapshots of the instantaneous mixture fraction at three different time instants obtained from the DNS are shown in Fig. 5. The mixture fraction is the most important representative variable in non-premixed combustion. Fig. 5(a1), (a2) and (a3) show the development of inner vortical structures for the disturbed non-buoyant case and its downward movement with respect to time. The asymmetric behaviour of the mixture fraction is also apparent at all three time instants and the mixture fraction distribution shifts more towards one direction when reaches the impinging wall for the non-buoyant case. The mixture fraction displays asymmetric vortical structures at the wall for the non-buoyant case due to the introduction of an asymmetric external disturbance. As seen in Fig. 5(b1), (b2) and (b3), the undisturbed buoyant case shows different

mixture fraction developments compared to the non-buoyant case. It can be seen that the buoyancy has a direct impact on the vortex topology of the impinging jet. For the buoyant case, the flow develops into large outer vortical structures in the primary jet stream, while vortical structures on the inner side of the primary jet stream are also visible. However, mixture fraction of the undisturbed buoyant case shows perfectly symmetric behaviour compared to the disturbed non-buoyant case. Compared with the undisturbed buoyant case, time evolution of the disturbed buoyant case exhibits asymmetric behaviour in both primary and wall jet regions.

Fig. 6 shows the instantaneous progress variable distributions of cases A, B and C at $t=8, 12$ and 16 . The progress variable is the most representative variable to describe the progress of the entire chemical reaction towards chemical equilibrium. Again, Fig. 6(a1), (a2) and (a3) display development of inner vortical structures in the absence of buoyancy, but with disturbance. For the non-buoyant case, the asymmetric behaviour of the progress variable is also exhibited at

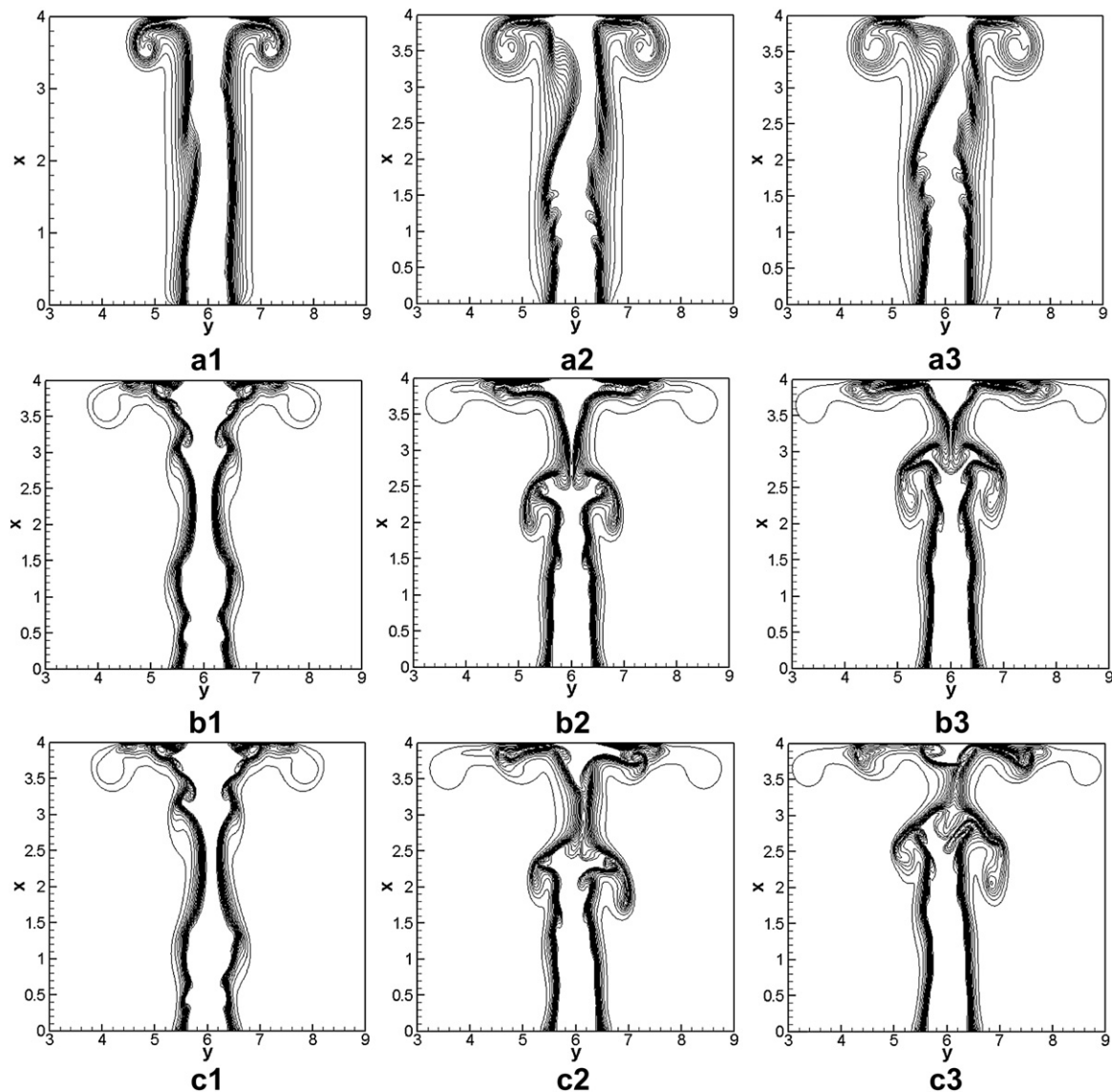


Fig. 5 – Instantaneous mixture fraction distributions of cases A, B and C at $t = 8$ (a1, b1, c1), $t = 12$ (a2, b2, c2) and $t = 16$ (a3, b3, c3).

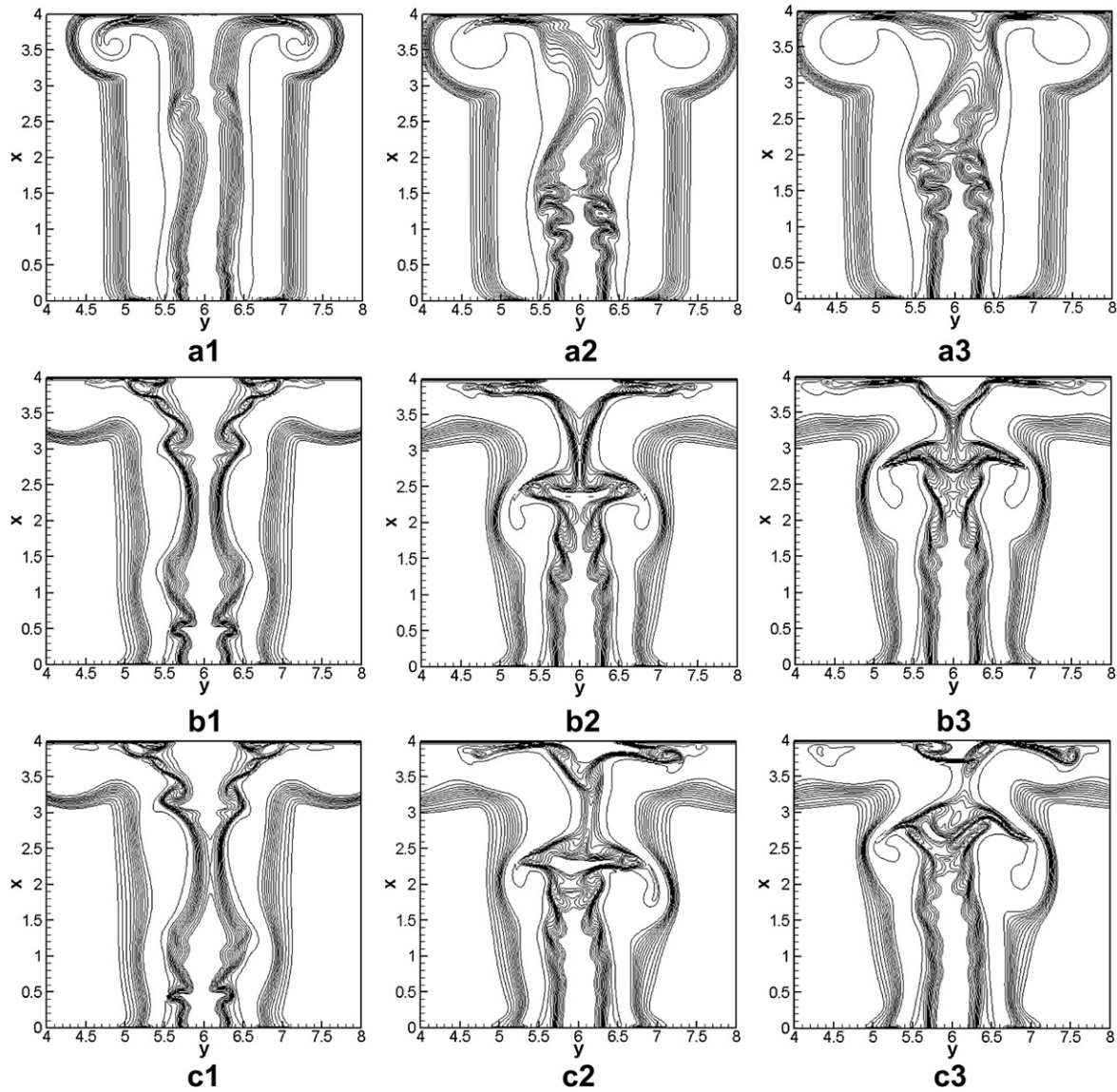


Fig. 6 – Instantaneous progress variable distributions of cases A, B and C at $t = 8$ (a1, b1, c1), $t = 12$ (a2, b2, c2) and $t = 16$ (a3, b3, c3).

all three time stages and the progress variable moves more towards one direction when reached the impinging wall. However, as seen in both buoyant cases, the strength of the inner vortical structures weakens in these cases, but the formation of large outer vortical structures dominates the flow field. These findings are also consistent with the literature [39,40] as the development of the inner vortical structures arises as a consequence of the growth of the inertial shear instability, while the formation of the outer vortical structures is due to buoyancy effects. Compared with the mixture fraction, the time development of the progress variable exhibits much clearer inner vortical structures in the primary jet for all three cases. In Fig. 6, the downstream movement of both inner and outer vortical structures of the primary jet and time evolution of the wall jet vortical structures follow similar behaviour to mixture fraction in terms of location and time.

The instantaneous temperature distributions obtained from the DNS results are shown in Fig. 7 for cases A, B and C at $t = 8, 12$ and 16 , respectively. The time evolution of the temperature distributions largely follows the mixture fraction behaviour, showing significant structural changes between the buoyant and non-buoyant cases. The non-buoyant case with disturbance exhibits inner vortical structures at the primary jet and its downward (streamwise) movement with time advancement. The asymmetric behaviour is also apparent for the temperature of the non-buoyant case. Again both buoyant cases exhibit weaker inner and much stronger outer vortical structures in the temperature field. Both inner and outer vortical structures of the temperature field are shifting downwards, and in addition, outer vortical structures spread radially with respect to time.

In general, there exists a preferred frequency for jets at which an axisymmetric disturbance receives maximum

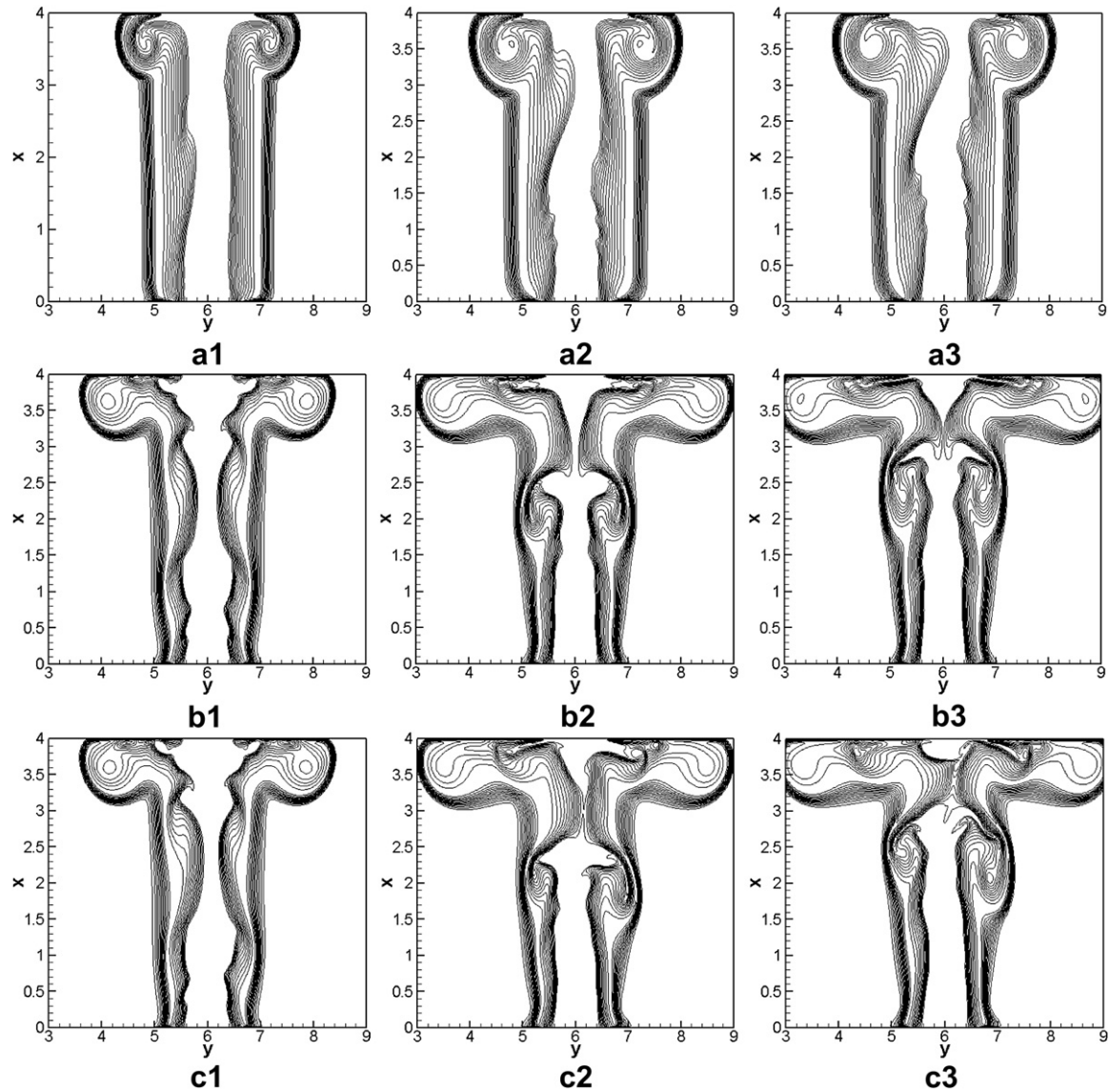


Fig. 7 – Instantaneous temperature distributions of cases A, B and C at $t = 8$ (a1, b1, c1), $t = 12$ (a2, b2, c2) and $t = 16$ (a3, b3, c3).

amplification in the jet column and the jet develops large-scale vortical structures [41]. In order to analyse the preferred frequency with and without buoyancy we constructed Fourier spectra by applying Fast Fourier Transform (FFT) for the instantaneous vertical velocity. Fig. 8 shows the Fourier spectra of the instantaneous streamwise velocity component at a streamwise distance $x = 2.3$. As seen in Fig. 8(a) the disturbed non-buoyant case has a highest peak at $St = 0.30$, which is the dominant frequency corresponding to the jet preferred mode of instability [42]. The undisturbed buoyant case has a dominant frequency at $St = 0.40$ with a similar amplitude as others (Fig. 8(b)). This frequency represents the flickering or puffing frequency of the buoyancy driven flow, which is close to the experimentally reported value of hydrogen flames [43,44]. However, as seen in Fig. 8(c), the disturbed buoyant case shows two dominant frequencies at $St = 0.30$ and $St = 0.50$ and these values are consistent with the previous investigations of combustion induced buoyancy and

jet preferred modes [42–44]. This is because of the complex interaction between the jet preferred mode and the buoyancy instability. However, further computational work of hydrogen flames with buoyancy effects for much higher Reynolds numbers and variable Froude numbers could reveal more details about effects of buoyancy relative to jet momentum as found by more recent experimental investigations [45,46] and this can be useful to refine the safety codes and standards for the future hydrogen based energy systems.

In the simulations performed in this study, it is worth noting that the flame showed a quasi-periodic behaviour at the later stage of the time-dependent simulations. The flames approximately exhibit a periodic behaviour in the primary jet stream, where large vortical structures are being formed and convected downstream continuously. Because of the relatively low speed of the flow in the wall boundary layer, the entire flow field did not reach a statistically stable stage at $t = 16$. Therefore the periods corresponding to the dominant

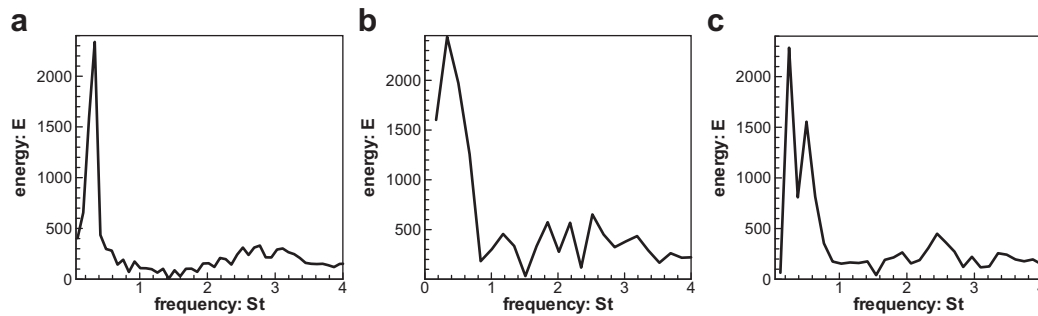


Fig. 8 – Fourier spectra of the instantaneous streamwise velocity variation at (2.3, 6.6, 6.0) of cases A, B and C.

frequencies shown in Fig. 8 are only representative for the specific location but not for the entire flow fields. Since the main objective of the study was to investigate the dynamic instabilities and near-wall behaviour of the reacting flow rather than to obtain accurate ensemble averaged results, the simulations were not extended to much longer durations which would require significantly larger computational costs. However, subsequent simulations of turbulent flows at a higher Reynolds number have been planned for much longer durations, where the ensemble averaged results are expected to be of more significant scientific value compared with the transitional flows simulated in this study.

For impinging flames, the near-wall heat transfer can be measured by the Nusselt number, which is a dimensionless number that measures the enhancement of heat transfer from a surface that occurs in a “real” situation, compared to the heat transfer that would be measured if only conduction could occur. The Nusselt number is used to measure the enhancement of heat transfer when convection takes place.

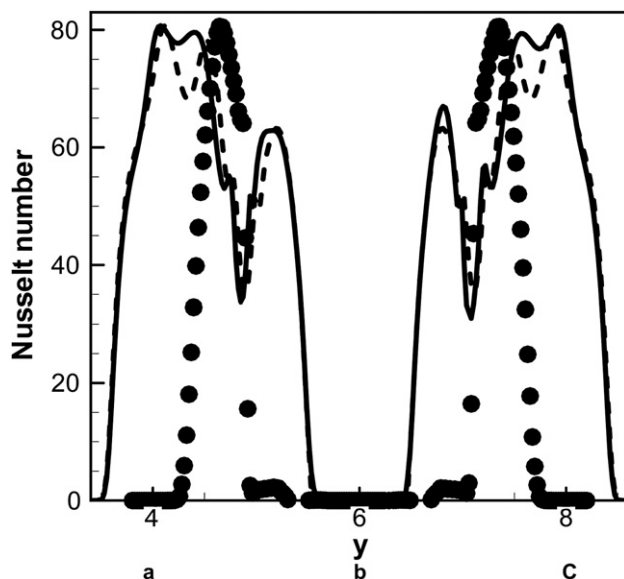


Fig. 9 – Instantaneous Nusselt number at the wall in the $z = 6.0$ plane at $t = 16$, here circles indicate disturbed non-buoyant case, dashed line indicates undisturbed buoyant case and solid line indicates disturbed buoyant cases, respectively.

Fig. 9 shows comparison of the instantaneous Nusselt number at $t = 16$ for cases A, B and C, corresponding to the instantaneous heat fluxes near the wall. Comparisons demonstrate that the buoyant cases have much wider temperature distribution and more fluctuations at the wall with respect to increasing radial distance from the wall stagnation point. The characteristics of Nusselt number distributions of impinging jet on flat plate are determined in several similar studies involving both laboratory experiments for high Reynolds number [47–49] and direct numerical simulations for low Reynolds number [50]. It is important to note that the Nusselt number distributions at the wall are found to be consistent with previous experimental and DNS studies and fluctuations of the Nusselt number are linked to the existence of vortical structures near the wall in the buoyant cases.

The temperature distributions indicate the existence of high flame temperature near the surface of the wall, which results in prominent near-wall heat transfer effects. Detailed discussion of the near-wall fluid flow, heat transfer and combustion phenomenon requires much more in-depth data analysis of the DNS results, which will be presented in subsequent efforts. Further analysis of mean wall heat flux such as averaged heat flux along the wall including surface chemistry effects and near-wall vorticity at the boundary layer should provide vital information on near-wall heat transfer for practical applications of hydrogen combustion.

6. Conclusions

Direct numerical simulation of reacting flows combined with flamelet generated manifold detailed chemistry was performed to investigate the vortical structures in hydrogen non-premixed impinging flames. Comparisons were made between three cases defined as disturbed non-buoyant, undisturbed buoyant and disturbed buoyant cases. It has been found that the inner vortical structures dominate the mixing of the primary jet for the non-buoyant case while the outer vortical structures dominate over the inner vortical structures in the flow fields of the buoyant cases. Buoyancy acted as an oscillator in the flow field and led to the formation of self-sustained outer vortical structures. The hydrogen flame driven by buoyancy was shown to have intrinsic flow instability as indicated by the results of the undisturbed buoyant case, which was highly unstable in nature. The external perturbation can further add to the

complexity of the vortical flow field. Vortex deformation occurs at the wall jet region due to the vortex-wall interaction. The comparisons between the buoyant flames and the non-buoyant flame revealed that the two flames have large differences at the primary jet region and impinging wall regions. Velocity variations and energy spectra demonstrate buoyancy effects on flame dynamics where the flow fields have very different dominant frequencies. It has been found that the dominant frequency of the undisturbed buoyant case is close to the experimentally observed flame flickering frequencies and the disturbed buoyant case had two dominant frequencies because of the complex interaction between the jet preferred mode and the buoyancy instability. Vortical structures are found to be the dominant feature of the flows investigated. These vortical structures affect the mixture fraction, progress variable and hence the flame temperature, which has been accounted for through the flamelet calculations. The unsteady vortex separation from the wall in the buoyant cases leads to variation in the Nusselt number distribution due to the changes in the instantaneous thermal boundary layer thickness.

More investigations on DNS of flame/wall interactions of hydrogen combustion will not only provide details about maximum wall heat flux distributions but also supply vital design guidelines for the next generation combustors for clean combustion bearing in mind that near-wall heat transfer determines the thermal loading of the combustor walls. The future DNS work will study the details of near-wall heat transfer including both the instantaneous and averaged wall heat fluxes as well as the effects of different wall boundary conditions, which will lead to the understanding of flame/wall interactions of hydrogen non-premixed impinging flames.

Acknowledgement

This research is funded by the UK EPSRC grant EP/G062714/2.

REFERENCES

- [1] Marban G, Valdes-Solfs T. Towards the hydrogen economy. *Int J Hydrogen Energy* 2007;32:1625–37.
- [2] Houf W, Schefer R. Predicting radiative heat fluxes and flammability envelopes from unintended releases of hydrogen. *Int J Hydrogen Energy* 2007;32:136–51.
- [3] Schefer RW. Hydrogen enrichment for improved lean flame stability. *Int J Hydrogen Energy* 2003;28:1131–41.
- [4] Coghe FCA. Behaviour of hydrogen enriched non-premixed swirl natural gas flames. *Int J Hydrogen Energy* 2006;31:669–77.
- [5] Schefer RW, Merilo EG, Groethe MA, Houf WG. Experimental investigation of hydrogen jet fire mitigation by barrier walls. *Int J Hydrogen Energy* 2011;36:2530–7.
- [6] Houf WG, Evans GH, Schefer RW, Merilo E, Groethe M. A study of barrier walls for mitigation of unintended releases of hydrogen. *Int J Hydrogen Energy* 2011;36:2520–9.
- [7] Heitsch M, Baraldi D, Moretto P. Numerical analysis of accidental hydrogen release in a laboratory. *Int J Hydrogen Energy* 2010;35:4409–19.
- [8] Heidari A, Ferraris S, Wen JX, Tam VHY. Numerical simulation of large scale hydrogen detonation. *Int J Hydrogen Energy* 2011;36:2538–44.
- [9] Schefer RW, Houf WG, Williams TC, Bourne B, Colton J. Characterisation of high-pressure, underexpanded hydrogen-jet flames. *Int J Hydrogen Energy* 2007;32:2081–93.
- [10] Owston R, Abraham J. Numerical study of hydrogen triple flame response to mixture stratification, ambient temperature, pressure, and water vapour concentration. *Int J Hydrogen Energy* 2010;35:4723–35.
- [11] TerMaath CY, Skolnik EG, Schefer RW, Keller JO. Emissions reduction benefits from hydrogen addition to midsize gas turbine feedstocks. *Int J Hydrogen Energy* 2006;31:1147–58.
- [12] Williams FA. Detailed and reduced chemistry for hydrogen autoignition. *J Loss Prev Process Ind* 2008;21:131–5.
- [13] Westbrook CK, Dryer FL. Chemical kinetic modelling of hydrocarbon combustion. *Prog Energy Combust Sci* 1984;10(1):1–57.
- [14] Saxena P, Williams FA. Testing a small detailed chemical kinetic mechanism for the combustion of hydrogen and carbon monoxide. *Combust Flame* 2006;145:316–25.
- [15] Zhang Y, Bray KNC. Characterisation of impinging jet flames. *Combust Flame* 1999;116:671–4.
- [16] Schuller T, Durox D, Candel S. Dynamics of and noise radiated by a perturbed impinging premixed jet flame. *Combust Flame* 2002;128:88–110.
- [17] Viskantha R. Heat transfer to impinging isothermal gas and flame jets. *Exp Therm Fluid Sci* 1993;6:111–34.
- [18] Wang Y, Trounev A. Direct numerical simulation of nonpremixed flame wall interactions. *Combust Flame* 2006;144:461–75.
- [19] Westbrook CK, Mizobuchi Y, Poinot TJ, Smith PJ, Warnatz J. Computational combustion. *Proc Combust Inst* 2005;30(1):125–57.
- [20] Anderson KR, Mahalingam S, Hertzberg J. A two-dimensional planner computational investigation of flame broadening in confined non-premixed jets. *Combust Flame* 1999;118:233–47.
- [21] Anderson KR, Mahalingam S. Numerical study of vortex flame interaction in actively forced non-premixed confined jets. *ASME J Heat Transfer* 2000;122:376–80.
- [22] Mahalingam S, Chen JH, Vervisch L. Finite rate chemistry and transient effects in direct numerical simulations of turbulent non-premixed flames. *Combust Flame* 1995;102:285–97.
- [23] Im HG, Chen JH. Effects of flow strain on triple flame propagation. *Combust Flame* 2001;126:1384–92.
- [24] Dabireau F, Cuenot B, Vermorel O, Poinot T. Interaction of flames of H₂/O₂ with inert walls. *Combust Flame* 2003;135:123–33.
- [25] Hawkes ER, Sankaran R, Sutherland JC, Chen JH. Scalar mixing in direct numerical simulations of temporally evolving plane jet flames with skeletal CO/H₂ kinetics. *Combust Flame* 2007;31:1633–40.
- [26] Yoo CS, Sankaran R, Chen JH. Three-dimensional direct numerical simulation of a turbulent lifted hydrogen jet flame in heated coflow: flame stabilisation and structure. *J Fluid Mech* 2009;640:453–81.
- [27] Gruber A, Sankaran R, Hawkes ER, Chen JH. Turbulent flame-wall interaction: a direct numerical simulation study. *J Fluid Mech* 2010;658:5–32.
- [28] Pitsch H. Shedding new light on a burning question. *J Fluid Mech* 2010;658:1–4.
- [29] van Oijen JA, de Goey LPH. Modelling of premixed laminar flames using flamelet-generated manifolds. *Combust Sci Technol* 2000;161:113–37.
- [30] Peters N. Reduced kinetic mechanisms and asymptotic approximations for methane-air flames. In: Smooke MD, editor. *Lecture notes in physics*, vol. 384. Berlin: Springer-Verlag; 1991. p. 48–85.

- [31] Maas U, Pope SB. Laminar flame calculations using simplified chemical kinetics based on intrinsic low-dimensional manifolds. *Proc Combust Inst* 1994;25:1349–56.
- [32] Massias A, Diamantis D, Mastorakos E, Goussis DA. An algorithm for the construction of global reduced mechanisms with CSP data. *Combust Flame* 1999;117:685–708.
- [33] Eggels RLGM, de Goeij LPH. Mathematically reduced mechanisms applied to adiabatic flat hydrogen/air flames. *Combust Flame* 1995;100:559–70.
- [34] Peters N. *Turbulent combustion*. Cambridge University Press; 2000.
- [35] Davis SG, Ameya VJ, Wang H, Egolfopoulos F. An optimised kinetic model of H_2/CO combustion. *Proc Combust Inst* 2005;30:1283–92.
- [36] Lele SK. Compact finite difference scheme with spectral-like resolution. *J Comput Phys* 1992;103:16–42.
- [37] Williamson JH. Low-storage Runge–Kutta schemes. *J Comput Phys* 1980;35:48–56.
- [38] Poinso TJ, Lele SK. Boundary-conditions for direct numerical simulations of compressible viscous flows. *J Comput Phys* 1992;101:104–29.
- [39] Katta VR, Roquemore WM. Role of inner and outer structures in transitional jet diffusion flame. *Combust Flame* 1993;92(3):274–82.
- [40] Katta VR, Goss LP, Roquemore WM. Numerical investigations of transitional H_2/N_2 jet diffusion flames. *AIAA J* 1994;32(1):84–94.
- [41] Hussain AKMF, Zaman KBMQ. The preferred mode of axisymmetric jet. *J Fluid Mech* 1981;110:39–71.
- [42] Gutmark E, Ho CM. Preferred modes and the spreading rates of jets. *Phys Fluids* 1983;26(10):2932–8.
- [43] Coats CM. Coherent structures in combustion. *Prog Energy Combust Sci* 1996;22:427–509.
- [44] Jiang X, Luo KH. Combustion-induced buoyancy effects of an axisymmetric reactive plume. *Proc Combust Inst* 2000;28:1989–95.
- [45] Schefer RW, Houf WG, Williams TC. Investigation of small-scale unintended releases of hydrogen: buoyancy effects. *Int J Hydrogen Energy* 2008;33:4702–12.
- [46] Schefer RW, Houf WG, Williams TC. Investigation of small-scale unintended releases of hydrogen: momentum-dominated regime. *Int J Hydrogen Energy* 2008;33:6373–84.
- [47] Viskanta R. Heat Transfer to impinging isothermal gas and flame jets. *Exp Therm Fluid Sci* 1993;6:111–34.
- [48] Lytle D, Webb B. Air jet impingement heat transfer at low nozzle-plate spacings. *Int J Heat Mass Transfer* 1994;37:1687–97.
- [49] Colucci D, Viskanta R. Effect of nozzle geometry on local convective heat transfer to a confined impinging air jet. *Exp Therm Fluid Sci* 1996;13:71–80.
- [50] Jiang X, Zhao Z, Luo KH. Direct numerical simulation of a non-premixed impinging jet flames. *ASME J Heat Transfer* 2007;129:951–7.